Optics Communications 410 (2018) 232–239

Contents lists available at ScienceDirect

Optics Communications

journal homepage: www.elsevier.com/locate/optcom

Analysis of the Sagnac interference imaging spectrometer with a variable optical path difference

Jingjing Ai [a], Peng Gao [a,b,*], Xiaochen Hu [a], Chunmin Zhang [b], Xia Wang [a,**]

[a] College of Mathematical and Physical sciences, Shandong Advanced Optoelectronic Materials and Technologies Engineering Laboratory, Qingtao University of Science and Technology, Qingdao 266061, China

[b] Institute of space Optics, School of Electronic and Information Engineering, Xi'an Jiaotong University, Xi'an 710049, China

ARTICLE INFO

Keywords:
Interference imaging spectrometer
Optical path difference
Wedge prism

ABSTRACT

The Sagnac interference imaging spectrometer with a variable optical path difference (OPD) is proposed in this paper, which employs two wedge prisms coupled with a modified Sagnac interferometer, and produces a variable OPD through the moving wedge prism. Compared with the conventional imaging spectrometer, the Sagnac interference imaging spectrometer shows its advantages of miniaturization and insensitive to the non-uniform variation of the moving speed and the environment vibration. The exact expression of the OPD as a function of different parameters is derived, and the influences of the moving displacement, wedge angle and acute angles on the OPD are analyzed and discussed within the scope of engineering design. This study provides an important theoretical and practical guidance for the engineering of the Sagnac interference imaging spectrometer.

1. Introduction

In recent years, people have developed a keen interest in the spectroscopic, multispectral or hyperspectral imaging spectrometer, which is widely used in astronomy, ballistic, fluorescent microscopy, remote sensing of the earth, and upper atmospheric winds and so on [1–5].

The most common interference imaging spectrometer has two categories: the temporarily modulated type and spatially modulated type. The temporarily modulated interference imaging spectrometer [6] is based on two-beam interference Michelson interferometer which changes the position of the system moving mirror to produce the OPD, thereby the time series of the interference data of the object can be obtained [7]. Due to the limit of the system slit, it is necessary for the temporarily modulated interference imaging spectrometer time to push a complete field of view to obtain the entire interferogram of the detection area [8,9].

To overcome the low real-time performance, the spatially modulated interference imaging spectrometer [10] is encouraged to be developed: one is based on the birefringent crystal as a spectrographic component [11–13]; another is based on the Sagnac interferometer [14,15]. These devices use a divided mirror to change the OPD and obtain simultaneously the interferogram of a list of object [16]. Nonetheless, the field of view and optical flux are still not enough, and the signal to noise ratio is not high, which means that the image quality needs to be improved [17]. Afterward, the tempo-spatially modulated polarization imaging interferometer is produced, which has the advantages of simple structure, large field of view, high flux and high resolution, and has an extremely broad application prospect [18–20].

The spectrometer based on the Sagnac interferometer can attain a high spectral resolution, but its OPD is not enough large [15]. This paper proposes the Sagnac interference imaging spectrometer as a novel device, whose core component is a modified Sagnac interferometer with a variable optical path difference (MSIVOPD). The MSIVOPD can achieve a larger OPD by the moving wedge prism, which is not so sensitive to the non-uniform variation of the moving velocity and environmental vibrations by choosing properly parameters. Besides, the construction and split-beam principle of the Sagnac interference imaging spectrometer are described in detail. The mathematical calculation and computer simulation are performed to demonstrate its characteristics and performances.

2. Principle of the Sagnac interference imaging spectrometer

The configuration of the Sagnac interference imaging spectrometer is depicted in Fig. 1, and its core component is the modified Sagnac interferometer with a variable OPD (MSIVOPD).

* Corresponding author at: College of Mathematical and Physical sciences, Shandong Advanced Optoelectronic Materials and Technologies Engineering Laboratory, Qingtao University of Science and Technology, Qingdao 266061, China.
** Corresponding author.
E-mail addresses: pgaoqust@163.com (P. Gao), phwangxia@163.com (X. Wang).

https://doi.org/10.1016/j.optcom.2017.10.027
Received 5 September 2017; Received in revised form 1 October 2017; Accepted 14 October 2017
Available online 5 November 2017
0030-4018/

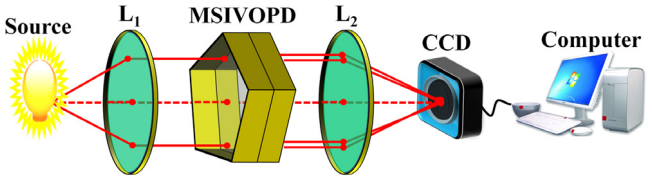

Fig. 1. The optical configuration of the Sagnac interference imaging spectrometer.

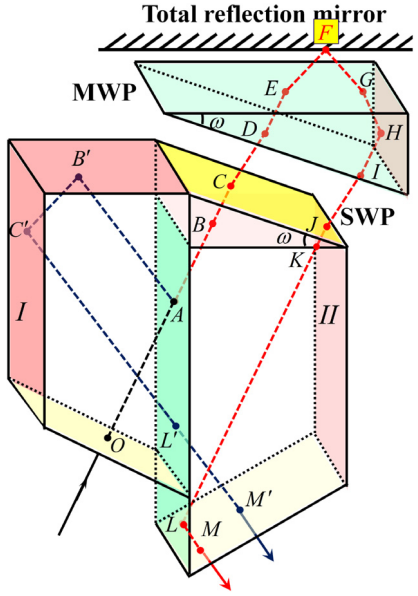

Fig. 2. The coordinate system of the MSIVOPD.

The MSIVOPD is composed of two right-angled trapezoid reflectors with the same refractive index, denoted by I and II, respectively, together with one stationary wedge prism (SWP) and one moving wedge prism (MWP), as shown in Fig. 2.

The right reflector drops a certain distance from the left along the cement surface coated with a semi-reflective multilayer, and the top and side of the left reflector are coated with the total reflection film as well as the sides of the right glass and the MWP. Besides, the SWP and MWP having the same wedge angle ω are made from the same material with refractive index n, and the long right angle side of the SWP is equal to the transverse length of the right reflector while the short right angle side is the same as the dislocation between I and II.

A bundle of light from the object is changed as the parallel beam by the collimating lens L_1 and vertically arrives at the incident surface of the MSIVOPD, and then one beam is split into two beams (one transmitted beam and one reflected beam) with the same intensity at the cement surface of the left–right reflectors. The transmitted beam passes through the SWP and MWP, then hits the total reflection mirror where it is reflected, after that, travels back to the right reflector, finally, goes through the exiting surface, while the reflected beam going out of the exiting surface by two reflections and one transmission. At the focal plane of the imaging lens L_2, these two components are reunited and an interference pattern can be generated by the overlapping collimating wavefronts. The image and interferogram of the object are recorded by the CCD detector, and then the spectral information can be obtained by the Fourier transform method.

3. Theoretical calculation of the OPD

When the MWP shifts along the direction of the right angle side or hypotenuse with equal displacement, different OPD can be produced, and the theoretical expression of the OPD is calculated and analyzed in the following parts.

3.1. MWP shifts along its right angle side

If the MWP shifts along its right angle side, the OPD introduced by the MSIVOPD is changed. Assume that the OPD is zero when the MWP is located at the position 0 denoted by the red solid line, and the OPD increases when the MWP being located at the position 1 indicated by the blue dashed line, as shown in Fig. 3(a).

Where a and b are the transverse lengths of I and II, and c is the dislocation between them; the acute angles of the left–right reflectors are β_1 and β_2, respectively.

According to the geometrical relationship $C_1D_1' = I_1'J_1'$ and $E_1'F_1' = F_1'G_1'$ in Fig. 3(a), if the MWP shifts from the position 0 to the position 1 and the moving distance is l, the OPD between the transmitted beam and reflected beam can be expressed as:

$$\begin{aligned}\Delta_1 = {} & \left(A_1B_1 + B_1C_1\right)n + 2C_1D_1' + D_1'E_1'n + 2E_1'F_1' + \left(G_1'H_1' + H_1'I_1'\right)n \\ & + \left(J_1'K_1' + K_1'L_1'' + L_1''M_1''\right)n - \left(A_1B_1' + B_1'C_1' + C_1'L_1' + L_1'M_1'\right)n.\end{aligned} \tag{1}$$

When the MWP is located at the position 0, the following condition is obtained:

$$\begin{aligned}& \left(A_1B_1 + B_1C_1\right)n + 2C_1D_1 + D_1E_1n + 2E_1F_1 + \left(G_1H_1 + H_1I_1\right)n \\ & + \left(J_1K_1 + K_1L_1 + L_1M_1\right)n = \left(A_1B_1' + B_1'C_1' + C_1'L_1' + L_1'M_1'\right)n.\end{aligned} \tag{2}$$

Letting L_1N_1 parallel to M_1M_1'', and $L_1''N_1'$ parallel to $J_1'J_1$, and taking Eq. (2) in to Eq. (1), the OPD is rewritten as:

$$\begin{aligned}\Delta_1 = {} & -2D_1'D_1 + \left(G_1'H_1' - G_1H_1 + H_1'I_1' - H_1I_1 + D_1'E_1'\right. \\ & \left. - D_1E_1 + L_1''N_1 - L_1N_1'\right)n.\end{aligned} \tag{3}$$

On the basis of the sine theorem, the following results are obtained from Fig. 3:

$$D_1'D_1 = s/\sqrt{1 - n^2\cos^2\left(\beta_1 + \omega\right)}, \tag{4}$$

$$\begin{aligned}G_1'H_1' - G_1H_1 = {} & \frac{\left[n\sin\left(\beta_1 + \omega\right) - \sqrt{1 - n^2\cos^2\left(\beta_1 + \omega\right)}\right]\cos\left(\beta_1 + \omega\right)s}{\sin\beta_1\cos\beta_1\sqrt{1 - n^2\cos^2\left(\beta_1 + \omega\right)}} \\ & - \frac{l}{\cos\beta_1},\end{aligned} \tag{5}$$

$$D_1'E_1' - D_1E_1 = \frac{\cos\omega\sqrt{1 - n^2\cos^2\left(\beta_1 + \omega\right)} - \sin\omega\cos\left(\beta_1 + \omega\right)n}{\sin\beta_1\sqrt{1 - n^2\cos^2\left(\beta_1 + \omega\right)}}s, \tag{6}$$

where s is the vertical distance between the hypotenuse at the positions 0 and 1, respectively, and $s = l\sin\omega$.

In the MWP and SWP, the following equations are satisfied:

$$H_1'I_1' - H_1I_1 = -\sin\beta_1\cos\omega\left(G_1'H_1' - G_1H_1\right)/\sin\left(\beta_1 + \omega\right), \tag{7}$$

and

$$\begin{aligned}J_1'J_1 = {} & \frac{l\left(1 + \sin\beta_1\right) + s\cos\left(\beta_1 + \omega\right)}{\sin\left(\beta_1 + \omega\right)} - \frac{ns\cos\left(\beta_1 + \omega\right)\left(1 + \frac{1}{\sin\beta_1}\right)}{\sqrt{1 - n^2\cos^2\left(\beta_1 + \omega\right)}} \\ & + \frac{s\cos\left(\beta_1 + \omega\right)}{\sin\beta_1\sin\left(\beta_1 + \omega\right)}.\end{aligned} \tag{8}$$

In the triangles $L_1L_1''N_1'$ and $L_1L_1''N_1$, using the Sine theorem, one has

$$L_1N_1' = \cos\omega L_1''N_1'/\cos\beta_1, \tag{9}$$

$$L_1''N_1 = \sin\beta_2\sin\left(\beta_1 + \omega\right)L_1''N_1'/\cos\left(\beta_1 - \beta_2\right)\cos\beta_1. \tag{10}$$

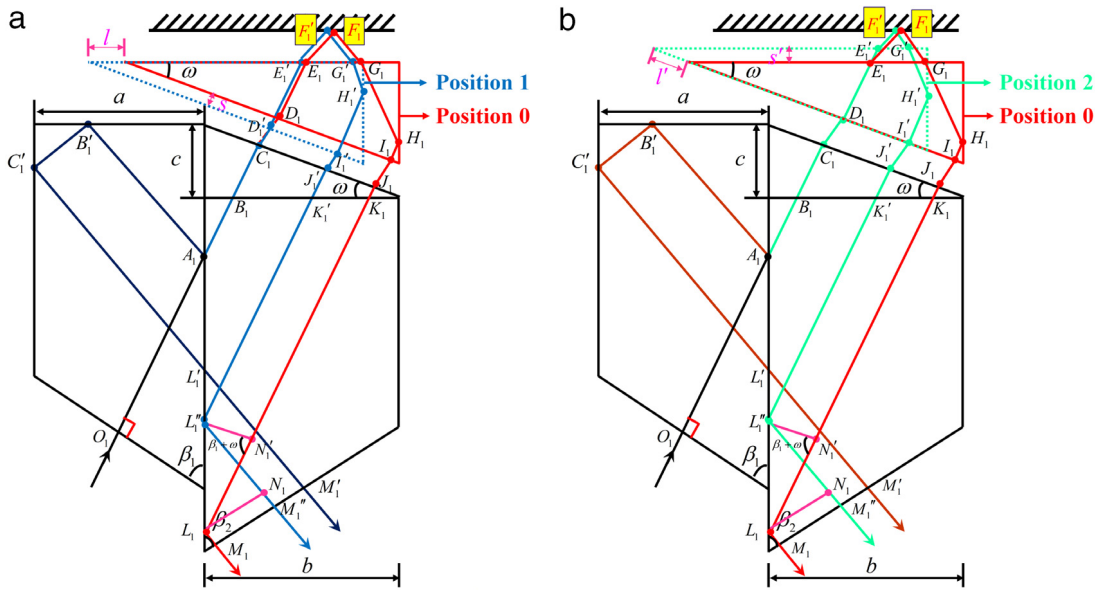

Fig. 3. The ray tracing of the MSIVOPD, where (a) the MWP shifting along its right angle side and (b) along its hypotenuse.

Substituting Eqs. (4)–(10) into Eq. (3), and using the relationship $L_1''N_1' = J_1'J_1$, the OPD is changed as:

$$\Delta_1 = -\frac{2l\sin\omega}{\sqrt{1-n^2\cos^2(\beta_1+\omega)}} - \frac{ln\cos(\beta_2+\omega)}{\cos(\beta_1-\beta_2)}\left[\begin{array}{c}\frac{(1+\sin\beta_1)}{\sin(\beta_1+\omega)}+\frac{\sin\omega(1+\sin\beta_1)}{\sin\beta_1\mathrm{tg}(\beta_1+\omega)}\\ -\frac{n\sin\omega\cos(\beta_1+\omega)\left(1+\frac{1}{\sin\beta_1}\right)}{\sqrt{1-n^2\cos^2(\beta_1+\omega)}}\end{array}\right]. \tag{11}$$

3.2. MWP shifts along its hypotenuse

When the MWP shifts from the position 0 to the position 2 along the hypotenuse, the OPD increases, and two positions are denoted by the red solid line and the green dash line, respectively, as shown in Fig. 3(b).

Similarly, when the MWP shifts the distance l' from the position 0 to the position 2, based on the geometrical relationship of Fig. 3(b), the OPD between the transmitted beam and reflected beam can be given by:

$$\Delta_2 = E_1'E_1 n + 2\left(E_1'F_1' - E_1F_1\right) + \left(G_1'H_1' - G_1H_1 + H_1'I_1' - H_1I_1 + L_1''N_1 - L_1N_1'\right)n. \tag{12}$$

Correspondingly, the following conditions can be obtained from Fig. 4:

$$E_1'E_1 = s'/\sin\beta_1, \tag{13}$$

$$E_1'F_1' - E_1F_1 = -s'/\sqrt{1-n^2\cos^2\beta_1}, \tag{14}$$

$$G_1'H_1' - G_1H_1 + H_1'I_1' - H_1I_1 = -\frac{l'\sin\omega\cos\omega}{\sin(\beta_1+\omega)} + \frac{s'n\cos\beta_1\cos\omega}{\sin(\beta_1+\omega)}\left[\frac{1+n\cos\beta_1}{\sqrt{1-n^2\cos^2\beta_1}} - \frac{\cos\beta_1}{\sin\beta_1}\right], \tag{15}$$

here s' is the vertical distance between the right angle side at the positions 0 and 2, respectively, and $s' = l'\sin\omega$.

Besides, the following equations are satisfied:

$$J_1'J_1 = \frac{4l'\sin\beta_1\cos\omega - l'\sin\omega\sin2\beta_1\left(1+n\cos\beta_1\right)\left(\frac{n}{\sqrt{1-n^2\cos^2\beta_1}} - \frac{1}{\sin\beta_1}\right)}{2\sin(\beta_1+\omega)}, \tag{16}$$

$$L_1''N_1 - L_1N_1' = -\cos(\beta_2+\omega)\,L_1''N_1'/\cos(\beta_1-\beta_2). \tag{17}$$

Substituting Eqs. (13)–(17) into Eq. (12), and using the relationship $L_1''N_1' = J_1'J_1$, the OPD is changed as:

$$\Delta_2 = \frac{n^2l'\left(1+n\cos\beta_1\right)\left[\sin2\omega\cos\beta_1 + \frac{\sin\omega\sin2\beta_1\cos(\beta_2+\omega)}{\cos(\beta_1-\beta_2)}\right]}{2\sin(\beta_1+\omega)\sqrt{1-n^2\cos^2\beta_1}} + \frac{nl'\sin\omega\left(\sin\omega - n\cos\omega\cos\beta_1\right)}{\mathrm{tg}\beta_1\sin(\beta_1+\omega)} - \frac{2l'\sin\omega}{\sqrt{1-n^2\cos^2\beta_1}} - \frac{nl'\cos(\beta_2+\omega)\left(2\sin\beta_1\cos\omega + \cos\beta_1\sin\omega - n\sin\omega\cos^2\beta_1\right)}{\sin(\beta_1+\omega)\cos(\beta_1-\beta_2)}. \tag{18}$$

3.3. Comparison of the OPDs along different directions

If the moving wedge prism make a displacement l, and it can be represented by $l = vt$, based on Eq. (11) and (18), the corresponding OPD is respectively written as:

$$\Delta_1 = G_1vt, \tag{19}$$

$$\Delta_2 = G_2vt. \tag{20}$$

Here G_1 and G_2 are the weights of the OPD along the right angle side and hypotenuse, respectively, while v and t represent the moving speed and time for the moving wedge prism.

So, the exact expressions of the weights for different OPD can be obtained:

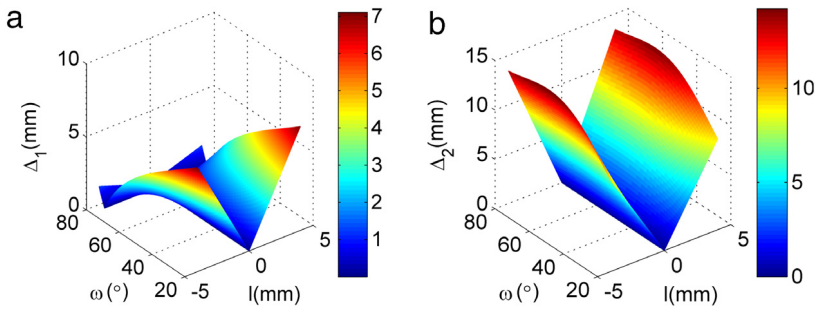

Fig. 4. The variations of the OPDs Δ_1 and Δ_2 changing with the wedge angle ω and moving displacement l for $\beta_1 = 40°$ and $\beta_2 = 50°$.

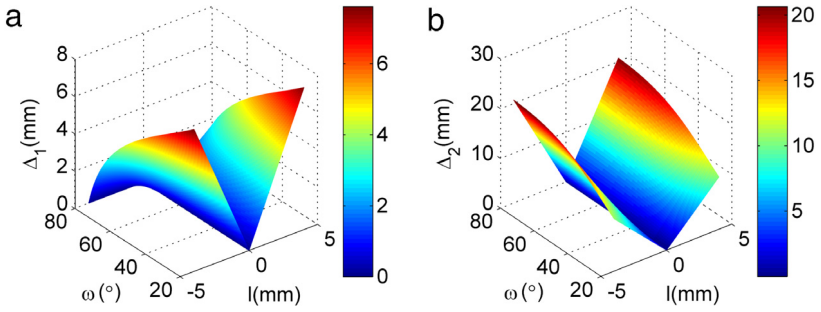

Fig. 5. The variations of the OPDs Δ_1 and Δ_2 changing with the wedge angle ω and moving displacement l for $\beta_1 = \beta_2 = 45°$.

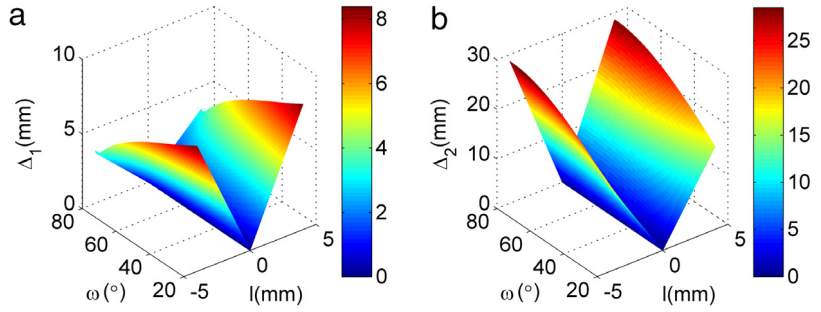

Fig. 6. The variations of the OPDs Δ_1 and Δ_2 changing with the wedge angle ω and moving displacement l for $\beta_1 = 50°$ and $\beta_2 = 40°$.

$$G_1 = -\frac{2\sin\omega}{\sqrt{1-n^2\cos^2(\beta_1+\omega)}} - \frac{n\cos(\beta_2+\omega)}{\cos(\beta_1-\beta_2)}\left[\begin{array}{c}\frac{(1+\sin\beta_1)}{\sin(\beta_1+\omega)}+\frac{\sin\omega(1+\sin\beta_1)}{\sin\beta_1\,\mathrm{tg}(\beta_1+\omega)}\\ -\frac{n\sin\omega\cos(\beta_1+\omega)\left(1+\frac{1}{\sin\beta_1}\right)}{\sqrt{1-n^2\cos^2(\beta_1+\omega)}}\end{array}\right], \tag{21}$$

$$G_2 = \frac{n^2(1+n\cos\beta_1)\left[\sin 2\omega\cos\beta_1+\frac{\sin\omega\sin 2\beta_1\cos(\beta_2+\omega)}{\cos(\beta_1-\beta_2)}\right]}{2\sin(\beta_1+\omega)\sqrt{1-n^2\cos^2\beta_1}} + \frac{n\sin\omega(\sin\omega-n\cos\omega\cos\beta_1)}{\mathrm{tg}\beta_1\sin(\beta_1+\omega)} - \frac{2\sin\omega}{\sqrt{1-n^2\cos^2\beta_1}} - \frac{n\cos(\beta_2+\omega)(2\sin\beta_1\cos\omega+\cos\beta_1\sin\omega-n\sin\omega\cos^2\beta_1)}{\sin(\beta_1+\omega)\cos(\beta_1-\beta_2)}. \tag{22}$$

From Eq. (21) and (22), it can be seen that different OPDs are produced due to different weights.

4. Computer simulation

In this part, the influences of different parameters on the OPD are demonstrated by a design example. Here, the MSIVOPD is provided with K9 glass, and its refractive index $n = 1.5148$ at a wavelength of 630 nm. During the simulation process, only two parameters are variable while other parameters keeping a constant.

4.1. Influences of the wedge angle and moving displacement on the OPD

Substituting the above parameters into Eqs. (11) and (18), the three-dimensional surfaces of the OPDs Δ_1 and Δ_2 changing with the wedge angle ω and moving displacement l are shown in Figs. 4–6, respectively. From Figs. 4–6, the distributions of the OPDs Δ_1 and Δ_2 are even symmetric to the axis $l = 0$, and the influence of the same moving displacement l on the OPD Δ_2 is larger than that of l on Δ_1, that is to say, the Sagnac interference imaging spectrometer can produce a larger OPD along the hypotenuse. With $\beta_1 = 50°$ and $\beta_2 = 40°$, the OPDs Δ_1 and Δ_2 have the maximum 8.394 mm and 28.540 mm, respectively, while Δ_1 and Δ_2 have the maximum 7.111 mm and 13.420 mm when $\beta_1 = 40°$ and $\beta_2 = 50°$. If the moving displacement l remains a constant, Δ_1 first increases rapidly then decreases slowly with the increasing of ω while the variation of Δ_2 changing with ω is just the opposite.

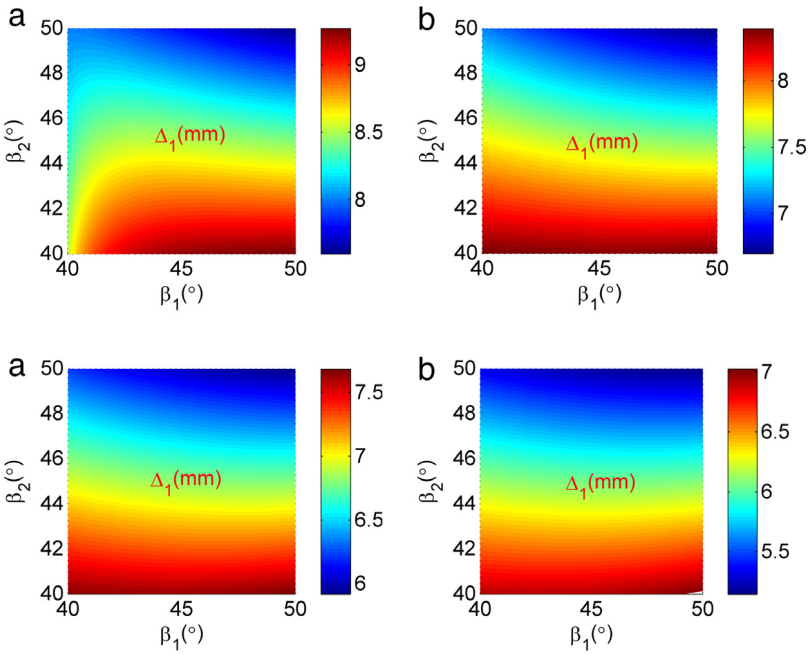

Fig. 7. The OPD Δ_1 as a function of the acute angles β_1 and β_2, where (a) $\omega = 10°$, (b) $\omega = 20°$, (c) $\omega = 30°$ and $\omega = 40°$, respectively.

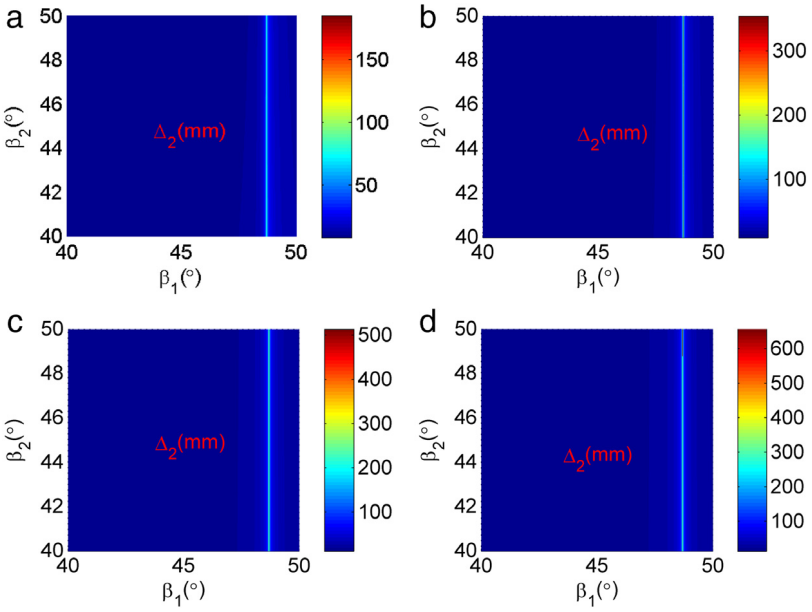

Fig. 8. The OPD Δ_2 as a function of the acute angles β_1 and β_2, where (a) $\omega = 10°$, (b) $\omega = 20°$, (c) $\omega = 30°$ and $\omega = 40°$, respectively.

In other words, choose an appropriate value for the wedge angle ω to make the instrument produce variable OPDs along two different directions. Besides, the increasing range of the OPD Δ with the moving displacement l is larger than that of Δ with the wedge angle ω, namely, the influence of the moving displacement on the OPD is more obvious.

4.2. Influences of the acute angles on the OPD

Assuming that the moving displacement $l = 4$ mm and the wedge angle ω is set as 10°, 20°, 30° and 40°, respectively, the three-dimensional plots of the OPDs Δ_1 and Δ_2 as a function of the acute angles β_1 and β_2 are displayed in Figs. 7 and 8. Where the horizontal axis and vertical axis represent β_1 and β_2, respectively, while the color distribution stands for the OPD values.

From Figs. 7 and 8, the variations of the OPDs have strong regularity and little clutter. The OPD Δ_1 decreases with the increasing of β_2 while it has little change with the various β_1. When the wedge angle increases, the variation of Δ_1 changing with β_1 is slower and slower. However, the OPD Δ_2 has almost no change with the increasing β_2, and it can arrive at the maximum when β_1 takes a certain value no matter what the value of β_2 is.

In order to further study the effects of the acute angles β_1 and β_2 on the OPD, a two-dimensional simulation is performed for the case $l = 4$ mm and $\omega = 10°$. According to Fig. 9, it is seen that, the distribution of Δ_1 in the upper boundary first increases rapidly, then changes slowly and reaches a maximum; the value of Δ_1 in the lower boundary decreases almost linearly with the increase of β_1 while its value in the middle part

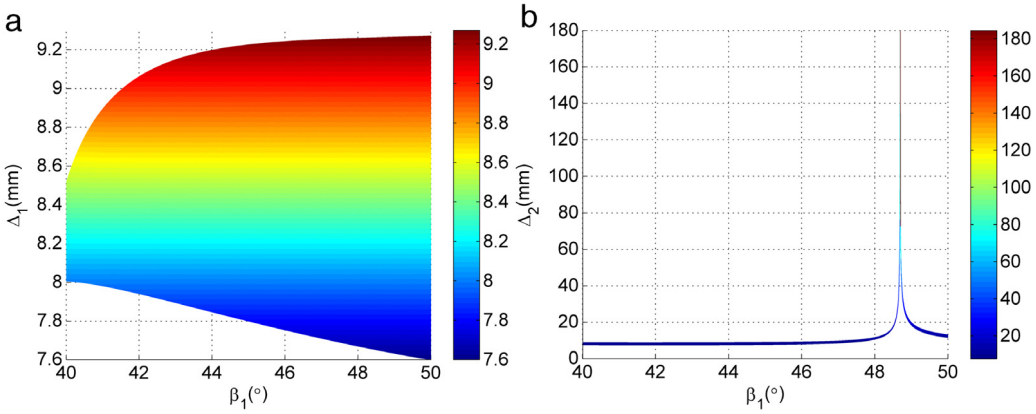

Fig. 9. The OPDs Δ_1 and Δ_2 as a function of the acute angle β_1 when β_2 keeps a constant.

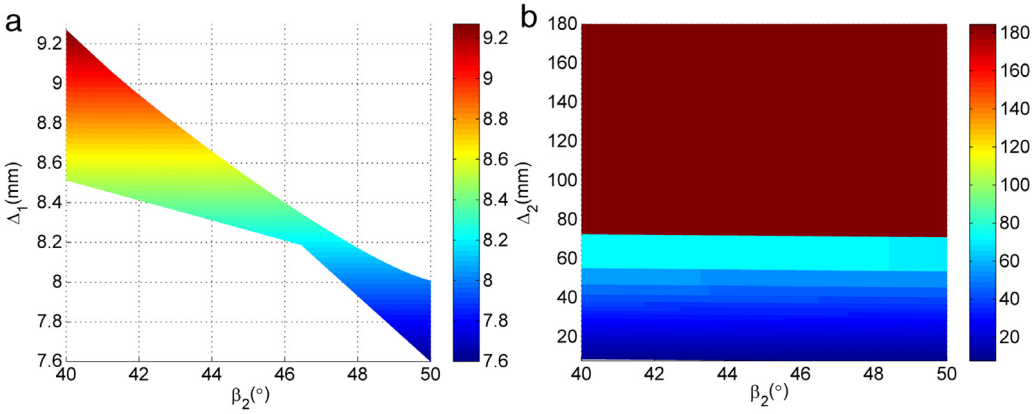

Fig. 10. The OPDs Δ_1 and Δ_2 as a function of the acute angle β_2 when β_1 keeps a constant.

has very little change; for the OPD Δ_2, it arrives at its maximum 76.28 mm when $\beta_1 = 48.68°$.

On the basis of Fig. 10, the distribution of the OPD Δ_1 in the upper boundary decreases with the increase of β_2. However, in the lower boundary, the value of Δ_1 first decreases slowly for $\beta_2 \in [40°, 46.25°)$, then decreases rapidly for $\beta_2 \in (46.25°, 50°]$ and reaches a minimum 7.6 mm. The OPD Δ_2 varies very little with β_2, and the difference between the maximum and minimum is less than 1.57 mm, that is to say, the influence on the OPD Δ_2 mainly comes from β_1.

According to the above analysis, the acute angle β_2 has a larger influence on Δ_1 and has no effect on Δ_2 when β_1 varying in the vicinity of 45 °. So, in order to design a symmetric MSIVOPD, the acute angles can be chosen as $\beta_1 = \beta_2 = 45°$.

4.3. Influences of the wedge angle and refractive index on the weight

According to Eq. (21) and (22), the weights G_1 and G_2 as a function of the wedge angle ω and refractive index n are plotted in Figs. 11 and 12, respectively. Based on Fig. 11, the weight G_1 linearly increases approximately with the refractive index n, while the weight G_2 first increases slowly for $n \leq 1.41$ and arrives at a maximum, afterward, it decreases drastically for $n > 1.41$ and reaches a stable state, thus the refractive index cannot be exceed this scope during designing stage. From Fig. 12, the weight G_1 decreases with the wedge angle ω of $[0°, 3.67°]$ and $[3.70°, 40°]$, and achieves a maximum and minimum when $\omega = 3.68°$ and 3.69°, respectively. The weight G_2 linearly decreases with the wedge angle ω when $\omega < 5.14°$, but increases when $\omega > 6.17°$, and it remains unchanged for $\omega \in [5.14°, 6.17°]$. In addition, the weights G_1 and G_2 is equal when $\omega = 10.34°$, and the larger weight can be obtained by choosing properly the values of ω and n.

4.4. Influence of the moving displacement on the intensity

Assuming that the wedged prisms are made from the glass K9 with its refractive index $n = 1.41$ at a wavelength of 630 nm, and the wedge angle is $\omega = 10°$. The intensities I_1 and I_2 as a function of the moving displacement l are represented in Figs. 12–14. As can be seen, the intensities I_1 and I_2 varies drastically with the displacement l in the case of $\beta_1 = 40°$ and $\beta_2 = 50°$, especially when $\beta_1 = 50°$ and $\beta_2 = 40°$, the intensity I_1 changes more drastically. However, for $\beta_1 = \beta_2 = 45°$, the intensities I_1 and I_2 varies slowly with the displacement l, namely, the sampling interferogram of the Sagnac interference imaging spectrometer is not so sensitive to the non-uniform variation of the moving speed and the environment vibration if the acute angles are designed as $\beta_1 = \beta_2 = 45°$.

5. Conclusion

A novel Sagnac interference imaging spectrometer based on the MSIVOPD is proposed in this paper, which utilizes low cost and readily available optical components to achieve variable OPD. By shifting the MWP along its right angle side and hypotenuse with the same displacement, different OPDs can be produced, and the exact expressions of the OPD as a function of different parameters are obtained. The influences of the moving displacement, wedge angle and acute angles on the OPD are analyzed and discussed by computer simulations, and the variable quality of Δ_2 is larger than that of Δ_1 for the same increment of l. Besides, the weights G_1 and G_2 is equal in the case of $\omega = 10.34°$, and the larger weight can be obtained by choosing properly the values of ω and n. In order to make the sampling interferogram not so sensitive to the non-uniform variation of the moving speed and the environment vibration,

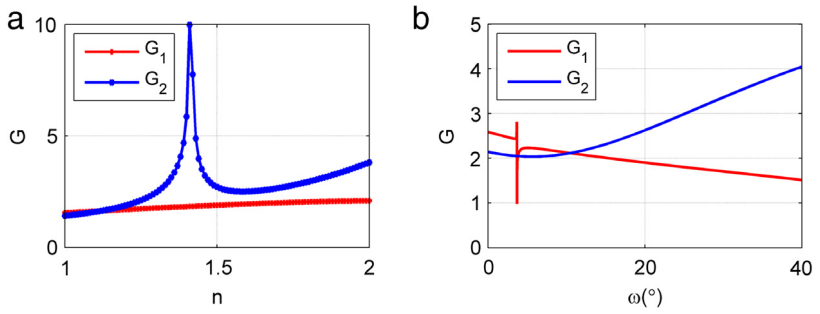

Fig. 11. The weights G_1 and G_2 as a function of the refractive index n and wedge angle ω for (a) $\omega = 10°$ and (b) $n = 1.5148$.

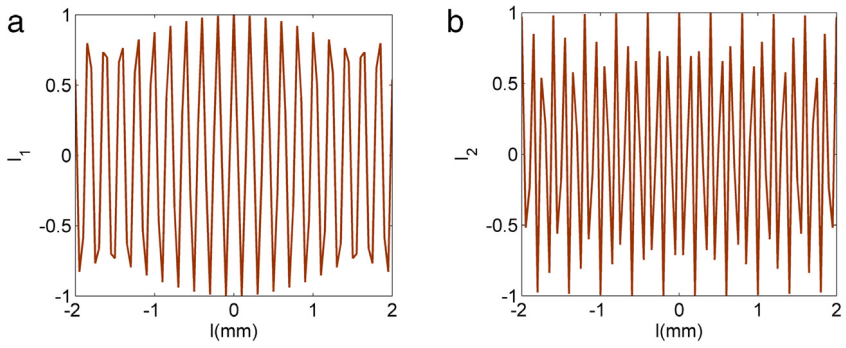

Fig. 12. The intensities I_1 and I_2 as a function of the moving displacement l for $\beta_1 = 40°$ and $\beta_2 = 50°$.

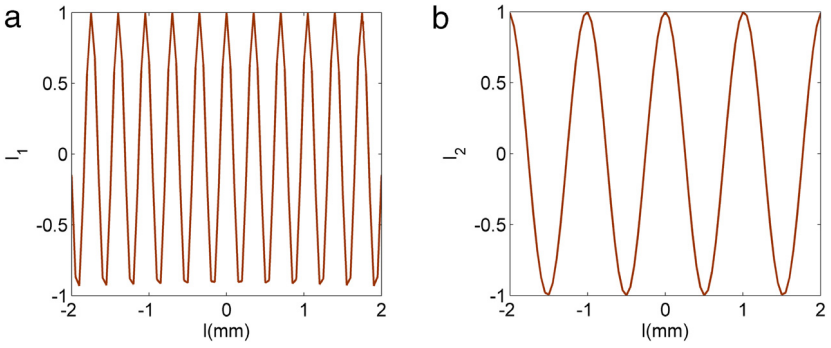

Fig. 13. The intensities I_1 and I_2 as a function of the moving displacement l for $\beta_1 = \beta_2 = 45°$.

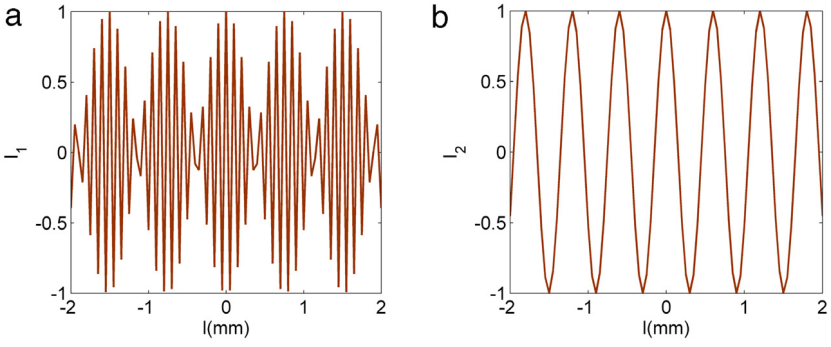

Fig. 14. The intensities I_1 and I_2 as a function of the moving displacement l for $\beta_1 = 50°$ and $\beta_2 = 40°$.

the acute angles of the Sagnac interference imaging spectrometer are designed as $\beta_1 = \beta_2 = 45°$.

Acknowledgments

The State Key Program of National Natural Science Foundation of China (41530422), the National Natural Science Foundation of China (61605098; 11704213), Natural Science Foundation of Shandong Province (ZR2017PD004).

References

[1] M.A. Folkman, Application of hyperspectral-imaging spectrometer systems to industrial inspection, 1996, 2599: 264-272.
[2] J.V. Lindner, D.A. Naylor, Simulation of the performance of ESA's Herschel/SPIRE imaging Fourier transform spectrometer, 2004, 5487: 469-480.
[3] M. Chamberl, V. Farley, J. Giroux, J.F. Legault, High-performance field-portable imaging radiometric spectrometer technology for hyperspectral imaging applications, Proc. Spie 5994 (2005) 169–179.
[4] D.A. Naylor, P. Roelfsema, M. Giard, F. Najarro, K. Wafelbakker, SAFARI: Imaging Spectrometer for the SPICA space observatory, Int. Soc. Opt. Photonics (2012) 489–498.
[5] P. Roelfsema, M. Giard, F. Najarro, K. Wafelbakker, W. Jellema, SAFARI new and improved: Extending the capabilities of SPICA's imaging spectrometer, in: Astronomical Telescopes + Instrumentation, 2014, p. 91431K.
[6] J.M. Preses, G.E. Hall, J.T. Muckerman, et al., Fourier-transform spectrophotometer for time-resolved emission measurements using a 100-point transient digitizer, Rev. Sci. Instrum. 64 (1) (1993) 95–102.
[7] H.H. Belz, F. Jede, B. Schrader, Infrared rotatory dispersion of induced cholesteric phases measured with a Fourier transform spectrophotometer, Appl. Spectrosc. 35 (3) (1981) 279–280.
[8] D.J.W. Kendall, H.L. Buijs, J.W.C. Johns, A very high resolution fourier transform spectrophotometer system for doppler-limited studies, J. Mol. Struct. 79 (1–4) (1982) 39–42.
[9] S.G. Kaplan, L.M. Hanssen, E.A. Early, M.E. Nadal, D. Allen, Comparison of near-infrared transmittance and reflectance measurements using dispersive and Fourier transform spectrophotometers, Metrologia 39 (2) (2002) 157.
[10] R.G. Sellar, J.B. Rafert, The effects of aberrations on spatially modulated Fourier transform spectrometers, Opt. Eng. 33 (9) (1994) 3087–3092.
[11] H.Y. Wu, C.M. Zhang, X. Bai, A complete description of polarization and transmission of nonnormal incident rays in a uniaxial birefringent plate with arbitrary optic axis, Opt. Commun. 283 (21) (2010) 4129–4134.
[12] T.K. Mu, C.M. Zhang, Models for polarization detection with the modified polarization interference imaging spectrometer, Optik-Int. J. Light Electron. Opt. 124 (7) (2013) 661–665.
[13] Q.Z. Cao, C.M. Zhang, E. Dehoog, Snapshot imaging polarimeter using modified savart polariscopes, Appl. Opt. 51 (24) (2012) 5791–5796.
[14] J.Y. Ye, C.M. Zhang, B.C. Zhao, Y.H. Tang, Optical path difference and detection mode of sagnac interferometer used for upper atmospheric detection, Acta Opt. Sin. 27 (7) (2007) 1145–1150.
[15] C.M. Zhang, J.J. Ai, P. Gao, Optical throughput of the sagnac interferometer with a modified large optical path difference, Appl. Opt. 51 (14) (2012) 2693–2700.
[16] R.A. Neville, L.X. Sun, K. Staenz, Detection of spectral line curvature in imaging spectrometer data, Proc. SPIE 5093 (144) (2003) 144–154.
[17] R.A. Neville, L.X. Sun, et al., Detection of keystone in imaging spectrometer data, Proc. SPIE 5425 (208) (2004) 208–217.
[18] C.M. Zhang, X.H. Jian, Wide-spectrum reconstruction method for a birefringence interference imaging spectrometer, Opt. Lett. 35 (3) (2010) 366–368.
[19] C.M. Zhang, Q.Z. Cao, X.H. Jian, W.Y. Ren, Image fusion of tempo-spatially modulated polarization interference imaging spectrometer, Opt. Commun. 297 (297) (2013) 12–19.
[20] C.M. Zhang, Q.W. Li, T.Y. Yan, T.K. Mu, Y.T. Wei, High throughput static channeled interference imaging spectropolarimeter based on a Savart polariscope, Opt. Express 24 (20) (2016) 23314.